Numerical study on the Leidenfrost behavior of a droplet stream impinging on a heated wall

Kshitiz Kumar Subedi [1] and Song-Charng Kong [2,*]

[1]*Department of Mechanical Engineering, Iowa State University, Ames, Iowa 50011, USA*
[2]*Department of Mechanical Engineering, Texas Tech University, Lubbock, Texas 79409, USA*

A detailed understanding of drop-wall interactions at high-temperature and high-pressure conditions can help optimize fuel injection, engine operation, and material design. The existing formulas developed for simulating drop-wall interactions are either valid only for a small range of operating conditions or based on the single-drop impact scenarios neglecting the effect of the nonstationary liquid film on the wall. The Leidenfrost temperature is a critical parameter in determining the impact outcome and needs to be considered in characterizing the impact behavior at extreme conditions. In this study, the smoothed particle hydrodynamics method, a Lagrangian-based method, is used to study the impact of an *n*-heptane droplet stream on a heated wall near and above the Leidenfrost temperature. The impingement frequency and wall temperature are varied to understand the impact dynamics and outcomes. Visualizations of the impact outcomes are provided to explain the interaction between the succeeding drops and the liquid film created by the preceding drops. To further characterize the shift in the Leidenfrost behaviors and the corresponding impact outcomes caused by the change in ambient pressure, simulations are also conducted at the corresponding fluid states for ambient pressures of 5 and 20 bar. Results show that the increase in ambient pressure impedes splashing and the film is concentrated inwards near the impingement point.

I. INTRODUCTION

The drop-wall interaction phenomenon presents a complex but important dynamics to comprehend because of its occurrence on film coating, spray cooling and quenching, inkjet printing, solidification, and fuel injection in combustion engines, to name a few. Postimpingement outcomes depend on impact energy, kinematic conditions, ambient conditions, wall surface temperature, surface roughness, and material. The impact dynamics of liquid drops on a heated piston surface at microscale under different ambient conditions requires investigations from the perspectives of hydrodynamics, heat transfer, and phase change. Understanding these impact behaviors and outcomes is pivotal, especially for ignition device design for engine applications under extreme operating conditions.

In drop-wall interactions, the heat-transfer regimes are mainly classified to include single-phase film evaporation, nucleate boiling, transition boiling, and film boiling [1–4]. The heat transfer from a heated wall to the liquid drop is characterized by the thermophysical properties of the solid-liquid pair in question. When the wall temperature is less than the saturation temperature of the liquid, the liquid remains in full contact with the wall (i.e., single-phase regime), where heat conduction and evaporation take place, thinning the film. As the wall temperature increases above the liquid's saturation temperature, vapor bubbles start to form, grow, and merge while the liquid drop is still in contact with the surface. This

phenomenon is known as nucleate boiling. As the wall temperature increases further, the lifetime of the drop decreases with the increase in the vaporization rate, and at one point, the evaporation time is minimum. This critical temperature is known as Nukiyama temperature. Nukiyama [5] studied the quantity of the heat transmitted from metal to boiling water under atmospheric pressure and introduced a critical temperature known as Nukiyama temperature (T_N), at which the lifetime of a drop is minimum. With a further increase in the wall surface temperature and the vaporization rate, a thin layer of vapor separates the drop from the surface. This reduces the heat flux from the wall to the drop, and the evaporation time increases until Leidenfrost temperature is reached, where the evaporation time is maximum. The Leidenfrost effect (as shown in Fig. 1) is a phenomenon in which the liquid drop hovers over the hot wall surface rather than making physical contact with the surface and wetting it because of the insulating thin film of vapor blanket that hinders the heat transfer from the hot surface to the drop. Beyond the Leidenfrost temperature, an increase in the wall temperature will increase the heat transfer across the vapor film to the drop due to conduction, causing the vaporization rate to increase.

The Leidenfrost temperature is an important parameter in drop-wall interactions as it determines the wetting regime. The Leidenfrost temperature can depend on liquid properties, droplet size, impact conditions, wall temperature, surface roughness, surface material, and ambient conditions. There are no universal formulas for determining the Leidenfrost temperature. The Leidenfrost temperature is mainly determined experimentally, and correlations have been formulated [6–9]
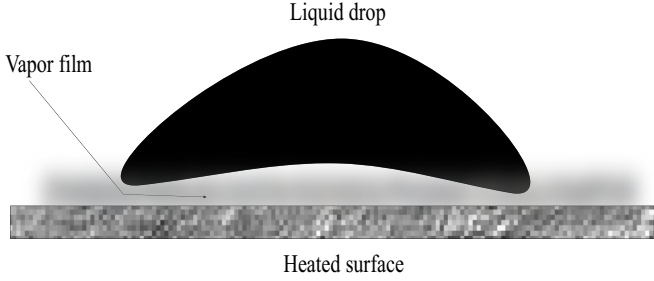
*sokong@ttu.edu

FIG. 1. Schematic of the Leidenfrost phenomenon during drop-wall impact.

based on experimental results. Bernardin and Mudawar [7] argued that the rise in the interfacial pressure due to droplet impact must be considered for determining the interfacial fluid properties; they provided a Leidenfrost-point model that accounts for the effect of impact velocity on the Leidenfrost temperature for a droplet. By combining the heat-transfer regimes and hydrodynamic behaviors, the outcomes of the single-drop impact have been categorized into four major regimes, namely deposition, contact splash, rebound, and film splash [10,11]. In the deposition regime, the liquid drop stays in contact with the surface and evaporates subsequently, whereas the liquid drop splashes and forms a thin liquid film on the surface in the contact splash regime. The rebound regime involves drop spreading, recoiling, and finally leaving the surface; film splash results in secondary droplets bouncing off and not in contact with the surface due to the vapor film.

Karl and Frohn [12] presented an experimental investigation of the interaction processes between small liquid droplets and hot walls above the Leidenfrost temperature. They provided correlations for loss of momentum and droplet deformation; they also studied the onset of droplet disintegration in the regime of secondary droplet formation. Moreira *et al.* [3] provided an extensive review on the study of spray-wall interactions focusing on single-drop impact; they highlighted the complexities of multiple droplet interactions. Cossali *et al.* [13] performed experiments of three water drops impacting simultaneously on a heated wall both below and above the Leidenfrost temperature; they compared the results with the single-drop case by measuring the secondary drop numbers and diameters and reported the occurrence of splashing even at low wall temperature conditions. Trujillo and Lewis [14] initialized the film to the saturation temperature and parametrically studied the heat-transfer characteristics in the boundary layer due to droplet train impingement without considering the phase change. Qiu *et al.* [15] investigated the splashing phenomenon of a high-speed water droplet train of water impinging on a heated surface and found that the spreading rate is enhanced at wall temperatures above the boiling point. Mundo *et al.* [16] provided a splashing criterion in terms of the K parameter $K = Oh \, \mathrm{Re}^{1.25}$, incorporating fluid properties and kinematic parameters. Yarin and Weiss (YW) [17] proposed a criterion by considering the kinematic discontinuity and crown formation to describe the impact of a droplet stream on a wall at a temperature below the saturation temperature as $u = U(\rho/\sigma)^{1/4} \nu^{-1/8} f^{-3/8}$. YW predicted that conditions $u \gtrsim 17$ would produce crown instability and

hence secondary droplets splashing. This criterion does not consider the effect of droplet diameter. Based on the YW findings, Stanton and Rutland [18] proposed a splashing criterion based on Weber number, i.e., splashing will occur for $We > 18^2 d(\rho/\sigma)^{1/2} \nu^{1/4} f^{3/4}$; this criterion incorporates the effects of droplet diameter. Liang and Mudawar [19] and Pan *et al.* [10] later verified that the K parameter proposed by Mundo *et al.* [16] provides a better prediction for the splashing dynamics than the Weber number alone.

A numerical study was conducted to characterize the impact of consecutive droplets on a wall whose temperature was lower than the droplet's saturation temperature, and the effects of impingement frequency were presented [20]. It was found that the effect of impingement frequency is seen as a kinematic discontinuity among the spreading lamellae, film formation, and rapidness of impact, and that the K parameter provides a better representation of the splashing dynamics. The findings on the impact of consecutive drops are consistent with those on the impact of an isolated drop.

Because of the difficulty in conducting experiments at high temperatures and high pressures, the existing formulas developed for simulating drop-wall interactions are either valid only for a small range of operating conditions or based on a single-drop impact scenario neglecting the effects of consecutive drops impinging on the nonstationary liquid film on the wall. To optimize fuel injection, engine operation, and material design at extreme conditions, it is fundamental to understand the drop-wall impact behavior at realistic engine conditions, e.g., high piston surface temperature. Extending the previous work on the droplet train impact at lower wall temperatures, the impact of a stream of *n*-heptane drops on a heated wall near and above the Leidenfrost temperature is studied in this paper. Different impingement frequencies are investigated to characterize the interaction among the drops. The shift in the Leidenfrost behaviors and corresponding impact outcomes due to the change in the ambient pressure are also investigated.

II. NUMERICAL METHOD

A. Governing equations

The Lagrangian form of unsteady, laminar Navier-Stokes equations and continuity equation of vapor species in the gas phase governing the drop-wall interaction process can be written as

$$\frac{D\rho}{Dt} = -\rho \boldsymbol{\nabla} \cdot \mathbf{u} + \dot{m}''', \tag{1}$$

$$\frac{D\mathbf{u}}{Dt} = \mathbf{g} - \frac{1}{\rho}\boldsymbol{\nabla}p + \frac{\mu}{\rho}\nabla^2\mathbf{u} + \boldsymbol{F}^S + \boldsymbol{F}^W, \tag{2}$$

$$\frac{DT}{Dt} = \frac{1}{\rho C_p}\boldsymbol{\nabla} \cdot (\kappa \boldsymbol{\nabla} T) - \frac{h_v}{\rho C_p}\dot{m}''', \tag{3}$$

$$\frac{DY}{Dt} = \frac{\boldsymbol{\nabla} \cdot (\rho D \boldsymbol{\nabla} Y)}{\rho}. \tag{4}$$

Here $\dot{m}'''$ is the volumetric mass evaporation rate across the liquid-gas interface, κ is the thermal conductivity, Y is the vapor mass fraction, D is the mass diffusivity, h_v is the latent heat of vaporization, $\boldsymbol{F}^S$ is the surface tension force, and $\boldsymbol{F}^W$ is

an artificial force between the liquid and the wall considering the effects of wall temperature and ambient pressure on drop rebound from the wall. Also, ρ, t, $\mathbf{u}$, $\mathbf{g}$, p, μ, T, and C_p are density, time, velocity, gravitational acceleration, pressure, dynamic viscosity, temperature, and specific heat at constant pressure, respectively. The volumetric mass evaporation rate across the liquid-gas interface is given by

$$\dot{m}''' = \frac{\nabla \cdot (\rho D \nabla Y)}{1 - Y}. \tag{5}$$

This term is added as a source term to the continuity equation, and its contribution to the energy equation during the phase change is also considered. Morris equation of state [21] is used to close the governing equations.

$$p = c^2(\rho - \rho_r) + p_r. \tag{6}$$

Here c is a numerical speed of sound, ρ_r is the reference density, and p_r is the reference pressure. The reference pressure used in this study is 1 bar. This equation of state ensures that the density fluctuation is below 1% such that the Mach number is less than 0.1 and the flow is incompressible. The choice of the speed of sound is guided by the balance of forces in momentum equations in which it should be large enough to ensure the incompressible behavior but small enough to avoid the need for a small time-step size.

B. Smoothed particle hydrodynamics formulation

The smoothed particle hydrodynamics (SPH) method is a meshless, Lagrangian particle-based method. The fundamental idea of the SPH method is to discretize the governing equations into SPH particle equations. The first step is to represent a field function $f(\mathbf{r})$ at point $\mathbf{r}'$ using integral function as

$$f(\mathbf{r}) = \int_\Omega f(\mathbf{r}')\delta(\mathbf{r} - \mathbf{r}')d\mathbf{r}', \tag{7}$$

where $\delta(\mathbf{r} - \mathbf{r}')$ is the Dirac delta function:

$$\delta(\mathbf{r} - \mathbf{r}') = \begin{cases} 1 & \mathbf{r} = \mathbf{r}' \\ 0 & \mathbf{r} \neq \mathbf{r}' \end{cases}. \tag{8}$$

This step is followed by the kernel approximation in which the Dirac delta function $\delta(\mathbf{r} - \mathbf{r}')$ is replaced with a smoothing function (or kernel) $W(\mathbf{r} - \mathbf{r}', h)$ where h represents the smoothing length connecting neighboring particles,

$$f(\mathbf{r}) \approx \int f(\mathbf{r}')W(\mathbf{r} - \mathbf{r}', h)d\mathbf{r}'. \tag{9}$$

Tensile instability may occur during SPH simulations for fluid flows and could result in the clustering of SPH particles and unphysical behaviors. To avoid the tensile instability using the SPH method, a hyperbolic-shaped smoothing function [22,23] proposed by Yang *et al.* is used:

$$W(s, h) = \alpha_d \begin{cases} s^3 - 6s + 6, & 0 \leqslant s < 1 \\ (2 - s)^3, & 1 \leqslant s < 2, \\ 0, & 2 \leqslant s \end{cases} \tag{10}$$

where $s = r/h$ and $\alpha_d = 15/(62\pi h^3)$ in 3D. Finally, to obtain the discretized SPH particle equations, the integral

representation of the field functions and their spatial derivatives are replaced with the summations over all the corresponding values of neighboring particles 'b' in the support domain. The following particle approximation forms are used in the present study:

$$f(\mathbf{r}_a) \approx \sum_b f(\mathbf{r}_b)W(\mathbf{r}_a - \mathbf{r}_b, h)\frac{m_b}{\rho_b}, \tag{11}$$

$$\nabla f_a = \rho_a \sum_b m_b \left(\frac{f_a + f_b}{\rho_a \rho_b}\right)\nabla_a W_{ab}, \tag{12}$$

$$\nabla \cdot \boldsymbol{f}_a = -\frac{1}{\rho_a} \sum_b m_b \boldsymbol{f}_{ab} \cdot \nabla_a W_{ab}, \tag{13}$$

$$\nabla^2 f_a = 2 \sum_b \frac{m_b}{\rho_b}(f_b - f_a)\Delta \boldsymbol{r}_{ab} \cdot \nabla_a W_{ab}. \tag{14}$$

Here, $\Delta \boldsymbol{r}_{ab} = \frac{\boldsymbol{r}_a - \boldsymbol{r}_b}{|\boldsymbol{r}_a - \boldsymbol{r}_b|^2}$, and $\nabla_a W_{ab} = \frac{\boldsymbol{r}_a - \boldsymbol{r}_b}{r_{ab}}\frac{\partial W_{ab}}{\partial r_{ab}}$ is the gradient of W taken with respect to the particle 'a'. With these formulations, the governing equations, Eqs. (1), (2), (3), and (4) become ordinary differential equations, which are then integrated in time using the explicit leapfrog method to obtain the numerical solutions.

$$\frac{D\rho_a}{Dt} = \sum_b m_b \mathbf{u}_{ab} \cdot \nabla_a W_{ab} + \dot{m}''', \tag{15}$$

$$\frac{D\mathbf{u}_a}{Dt} = \mathbf{g} - \sum_b m_b \left(\frac{p_a + p_b}{\rho_a \rho_b} + \Pi_{ab}\right)\nabla_a W_{ab}$$
$$+ \sum_b \frac{2m_b \bar{\mu}_{ab}\mathbf{r}_{ab} \cdot \nabla_a W_{ab}}{\rho_a \rho_b(r_{ab}^2 + \eta)}\mathbf{u}_{ab} + \boldsymbol{F}_a^S + \boldsymbol{F}_a^W, \tag{16}$$

$$\frac{DT_a}{Dt} = \frac{1}{C_p} \sum_b \frac{2m_b \bar{\kappa}_{ab}\mathbf{r}_{ab} \cdot \nabla_a W_{ab}}{\rho_a \rho_b(r_{ab}^2 + \eta)}T_{ab} - \frac{h_v}{\rho C_p}\dot{m}''', \tag{17}$$

$$\frac{DY_a}{Dt} = \sum_b \frac{m_b(\rho_a D_a + \rho_b D_b)\mathbf{r}_{ab} \cdot \nabla_a W_{ab}}{\rho_a \rho_b(r_{ab}^2 + \eta)}Y_{ab}, \tag{18}$$

$$\mathbf{u}_{ab} = \mathbf{u}_a - \mathbf{u}_b, \quad \mathbf{r}_{ab} = \mathbf{r}_a - \mathbf{r}_b,$$
$$T_{ab} = T_a - T_b, \quad Y_{ab} = Y_a - Y_b, \quad \eta = 0.01h^2, \tag{19}$$

$$\bar{\kappa}_{ab} = \frac{2\kappa_a \kappa_b}{\kappa_a + \kappa_b}, \quad \bar{\mu}_{ab} = \frac{2\mu_a \mu_b}{\mu_a + \mu_b}. \tag{20}$$

The term Π in Eq. (16) is an artificial viscosity [24] added to the pressure term to prevent the sharp variations in the flow and particle penetration, and is given by

$$\Pi_{ab} = \begin{cases} \frac{-\alpha \bar{c}_{ab}\mu_{ab} + 2\beta \mu_{ab}^2}{\bar{\rho}_{ab}}, & \mathbf{u}_{ab} \cdot \mathbf{r}_{ab} < 0 \\ 0, & \mathbf{u}_{ab} \cdot \mathbf{r}_{ab} \geqslant 0 \end{cases}, \tag{21}$$

where

$$\mu_{ab} = \frac{h\mathbf{u}_{ab} \cdot \mathbf{r}_{ab}}{r_{ab}^2 + \eta}, \quad \bar{c}_{ab} = \frac{c_a + c_b}{2}, \quad \bar{\rho}_{ab} = \frac{\rho_a + \rho_b}{2}. \tag{22}$$

The SPH formulation of the volumetric mass evaporation rate is given by

$$\dot{m}''' = \sum_L \frac{2\rho_G m_L D_G(\mathbf{r}_G - \mathbf{r}_L) \cdot \nabla_G W_{GL}}{\rho_L(r_{GL}^2 + \eta)(1 - Y_G)}Y_{GL}, \tag{23}$$

where the subscripts L and G denote the liquid and gaseous SPH particles, respectively. The continuum surface force

Properties and parameters	Value
Density	680 kg/m³
Surface tension	0.02 N/m
Dynamic viscosity	0.0004 Pa s
Drop diameter	50 μm
Impact velocity	10 m/s
Initial drop temperature	298 K
Weber number	170
Reynolds number	850
K parameter ($K = Oh$ Re$^{1.25}$)	70.4

model [25] defines the body force due to surface tension as

$$\boldsymbol{F}^S = \sigma \kappa \mathbf{n} \delta^S / \rho, \qquad (24)$$

where σ is the coefficient of surface tension, κ is the surface curvature, $\boldsymbol{n}$ is a unit vector normal to the surface, and δ^S is a delta function. The SPH formulation of this surface tension force can be written as

$$\boldsymbol{F}^S_a = -\frac{\sigma d}{V_a} \frac{\sum_b (\mathbf{n}_a - \mathbf{n}_b) \cdot V_b \nabla_a W_{ab}}{\sum_b |(\mathbf{r}_a - \mathbf{r}_b) \cdot V_b \nabla_a W_{ab}|} \sum_b \frac{V_a^2 + V_b^2}{\rho_a + \rho_b} \nabla_a W_{ab}, \qquad (25)$$

where d is the number of spatial dimensions, and V is the volume of an SPH particle. The artificial force $\boldsymbol{F}^W$ is used

when the wall temperature exceeds the boiling temperature of the liquid to mimic the force due to the vapor generated at the liquid-solid interface under high-temperature and high-pressure conditions. This force is given by

$$\boldsymbol{F}^W = f(T_W, P_{amb}) \frac{p_r}{\rho_L \rho_W} \boldsymbol{\nabla}_L W_{LW}, \qquad (26)$$

$$f(T_W, P_{amb}) = C^W (T^{*2} - 1) \frac{P^* + 1}{2},$$

$$T^* = T_W / T_B, \quad P^* = P_{amb} / P_{atm}, \qquad (27)$$

where T_w, T_B, P_{amb}, P_{atm}, and p_r are wall temperature, boiling temperature, ambient pressure, atmospheric pressure, and reference pressure, respectively. $C^W = 0.9$ is a coefficient used in the present study. The subscripts L and W denote the liquid and wall SPH particles, respectively. Further details of these forces are found in the previous work [26]. Equation (18) is solved only for a gaseous SPH particle which has a property of vapor mass fraction Y. Here, a gaseous SPH particle is a mixture of vapor and air, and at the liquid-gas interface, a liquid SPH particle is treated as a gaseous SPH particle with its vapor mass fraction defined by saturated vapor mass fraction [26,27].

Using an artificial equation of state to compute the pressure field may result in an error in density calculation accrued with the evolution in time. To minimize large numerical fluctuations that may occur during the SPH simulation, the Shepard filtering [28] is applied to reinitialize the density field after the
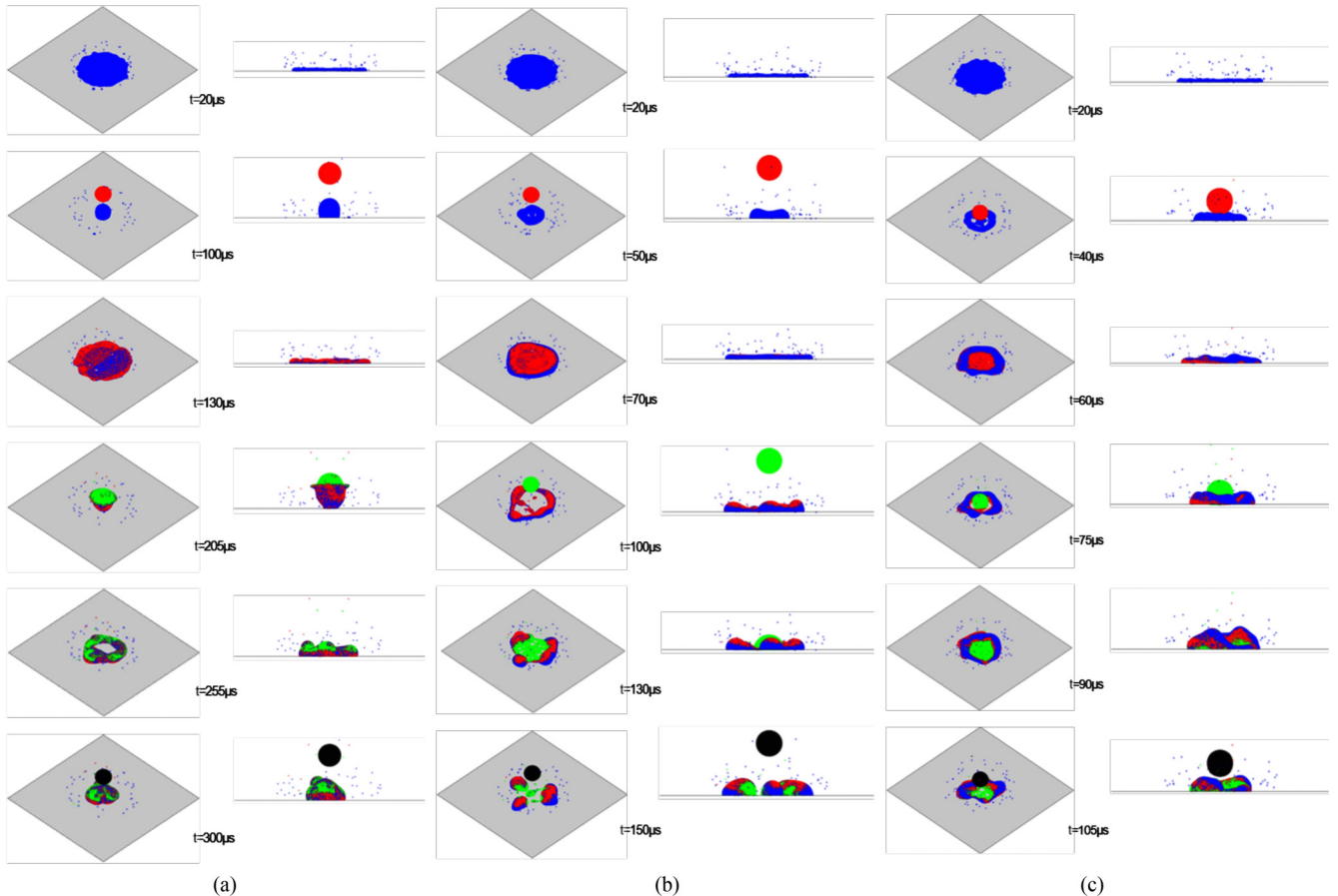

FIG. 2. Postimpingement outcomes at $T_w = 420$ K: (a) $f = 10$ kHz; (b) $f = 20$ kHz; and (c) $f = 30$ kHz.
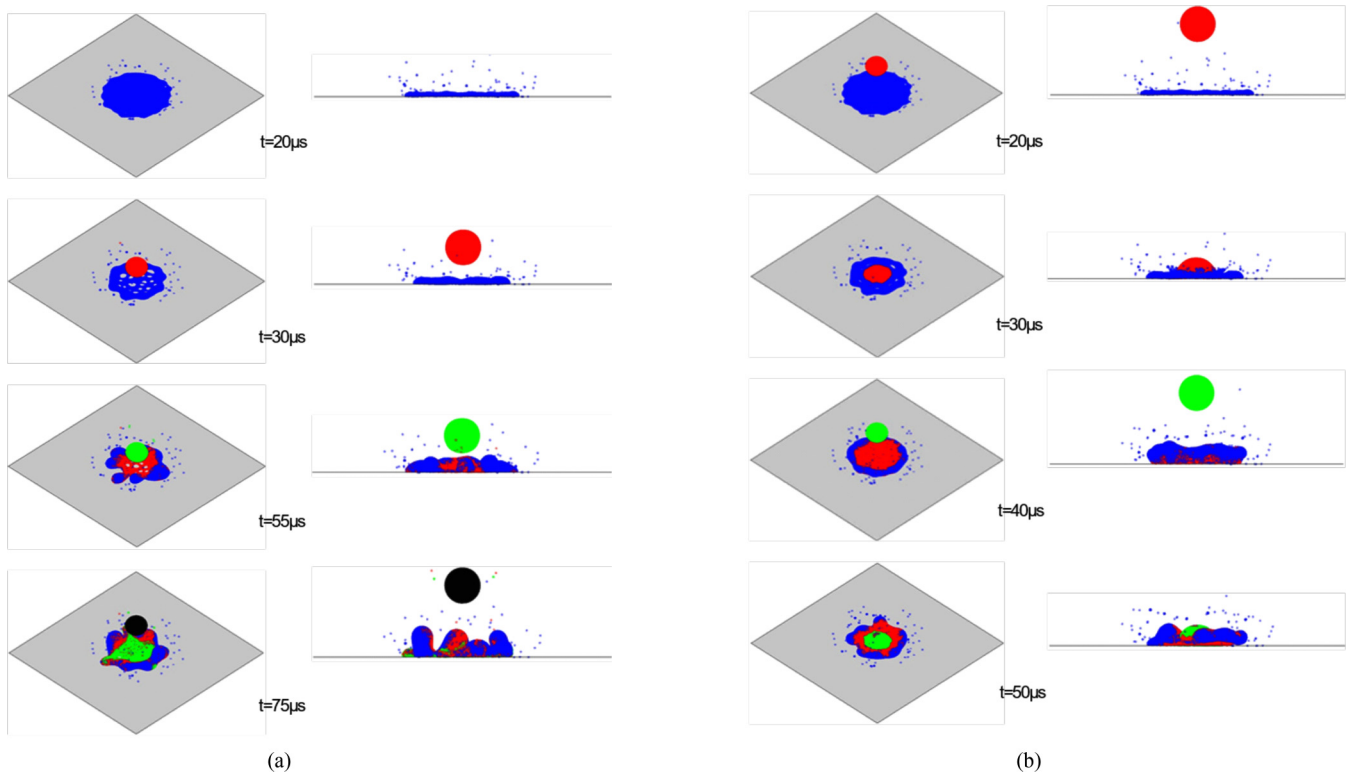
FIG. 3. Postimpingement outcomes at $T_w = 420$ K: (a) $f = 40$ kHz and (b) $f = 50$ kHz.
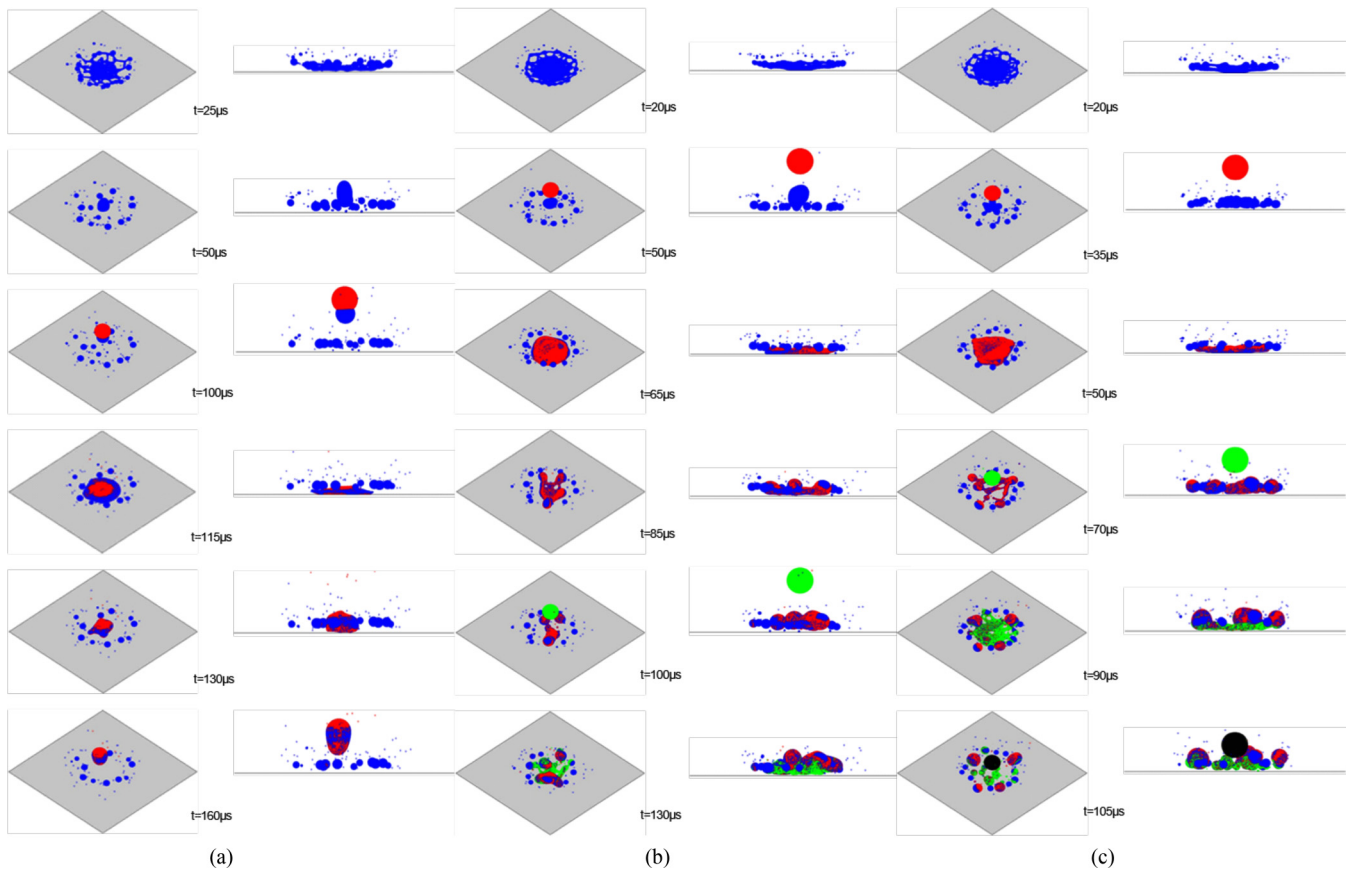

FIG. 4. Postimpingement outcomes at $T_w = 600$ K: (a) $f = 10$ kHz; (b) $f = 20$ kHz; and (c) $f = 30$ kHz.
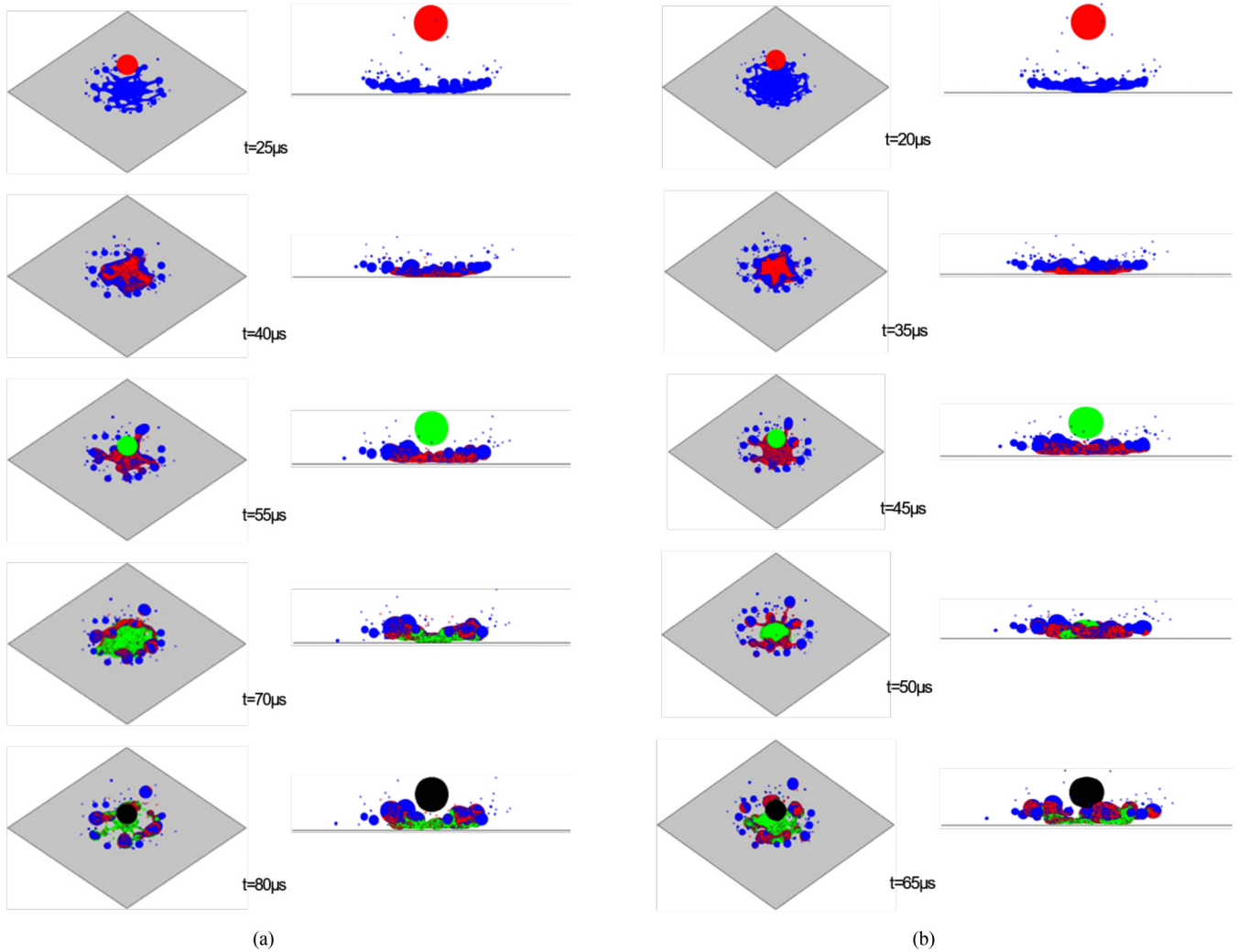
FIG. 5. Postimpingement outcomes at $T_w = 600$ K: (a) $f = 40$ kHz and (b) $f = 50$ kHz.

user-defined time steps.

$$\widetilde{\rho}_a = \frac{\sum_b m_b W_{ab}}{\sum_b V_b W_{ab}}. \tag{28}$$

In incompressible flows, the XSPH technique by Monaghan [24] incorporates the contribution from neighboring SPH particles. It is used to smooth out the obtained velocities using the average velocity of neighboring particles so that the movement of the particles is orderly.

$$\frac{d\mathbf{r}_a}{dt} = \mathbf{u}_a + \varepsilon \sum_b \frac{2m_b}{\rho_a + \rho_b}(\mathbf{u}_b - \mathbf{u}_a)W_{ab}. \tag{29}$$

III. RESULTS AND DISCUSSION

A. Impact outcomes

The present SPH method has been validated for the impacts of a single drop on the wall [10,26,27,29,30]. The present method has also been validated for crown rim propagation [20] against the experimental studies for the droplet train impact of ethanol [17] and Novec HFE-7100 [31] at different impingement frequencies. The wall temperatures used in these experimental works are lower than the saturation temperature of the liquid drop. The previous study [20] also characterizes the effects of the impingement frequency, droplet diameter, and ambient pressure on the impact outcome using n-heptane for wall temperature lower than the saturation temperature of the liquid drop. To further characterize the effects of wall temperature, the present study is focused on the impact of a stream of n-heptane drops at five different impingement frequencies (10, 20, 30, 40, and 50 kHz) and at wall temperatures near and above the Leidenfrost temperature. n-Heptane is chosen because it is a simple single-component n-alkane representation of diesel fuel. Both diesel fuel and n-heptane have similar ignition characteristics, i.e., cetane number, in diesel combustion applications. The heat-transfer regimes and impact outcomes of a single-drop impact on a dry surface guide our selection of wall temperatures (371, 420, 480, 600, and 750 K). Still, only the results from 420 K (below the Leidenfrost temperature) and 600 K (above the Leidenfrost temperature) are presented here for brevity. The properties of the n-heptane drop, and impact conditions used in this study are shown in Table I.

The computational domain was $4.5D \times 4.5D \times 3.0D$, which was chosen to save computer time without compromising the ability to capture the physics. Each drop was initialized
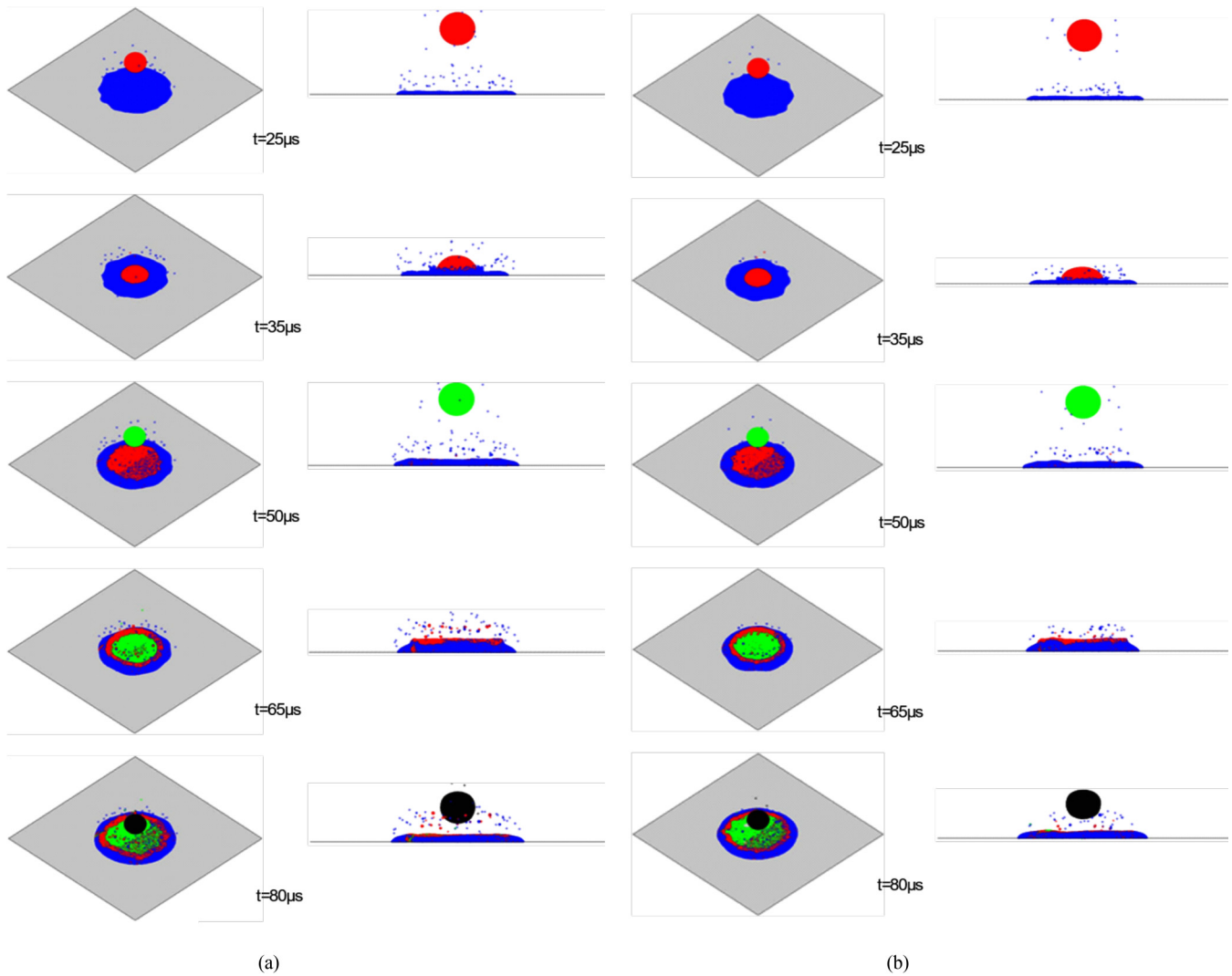
FIG. 6. Postimpingement outcomes at $T_w = 420$ K and $f = 40$ kHz: (a) $P = 5$ bar and (b) $P = 20$ bar.

at a height of $(2.5D - 12 \times ds)$, and the drop was generated in a time corresponding to the impingement frequency at the same location. Here D is the diameter of the drop, and ds is the spacing between two SPH numerical particles which is used to control the resolution of the liquid drop. For the present simulations, a spacing of 2×10^{-6} m was used; the total number of SPH particles representing a single liquid drop was 7825. The same spacing was used for gaseous and wall SPH particles, and the total number of SPH particles including the liquid drop was about $3.3M$. Dynamic boundary conditions were used for the solid wall boundary. To prevent liquid accumulation from affecting the impingement outcomes, the secondary droplets and liquid film were allowed to leave the domain from the side boundaries. Following Morris *et al.* [21], the artificial speed of sound $c = 240$ m/s was used in the equation of state for balancing between the time-step size and the incompressible behavior of an artificial compressible fluid. The time-step size used was 8×10^{-10} s.

For wall temperature 420 K, the impingement of the first drop produces a few secondary droplets from the rim at the time of impact. The drop spreads, reaches a maximum diameter, and then recoils. For the impingement at temperatures

above the saturation temperature of the drop (371 K), the drop recoils at a faster rate and tends to rebound. Despite such a tendency, the drop does not rebound but remains in contact with the wall. At the impingement frequency of 10 kHz shown in Fig. 2(a), the succeeding drops are generated at an interval of 100 μs. The second drop, impinging at the same impingement point, finds a nearly spherical drop-shaped film. On impingement, the drop merges into the film and spreads together. The merged film again recoils and takes the shape of a drop that is about to rebound. The successive impingement of succeeding drops further increases the size of the recoiling film, as seen in Fig. 2(a) at $t = 300$ μs.

The increase in the impingement frequency does not allow enough time for the film to recoil to attain a spherical shape. As shown in Fig. 2(b) and Fig. 2(c), the films subjected to the second drop impact are different from what is seen for $f = 10$ kHz. Some parts of the wall surface are also exposed for the incoming drop. The second drop spreads together with the film on the wall, but the liquid resulting from the second drop is concentrated toward the center. The impingement of subsequent drops finds the wall surface and traces of such liquid films. Part of the liquid drop vaporizes, and some other
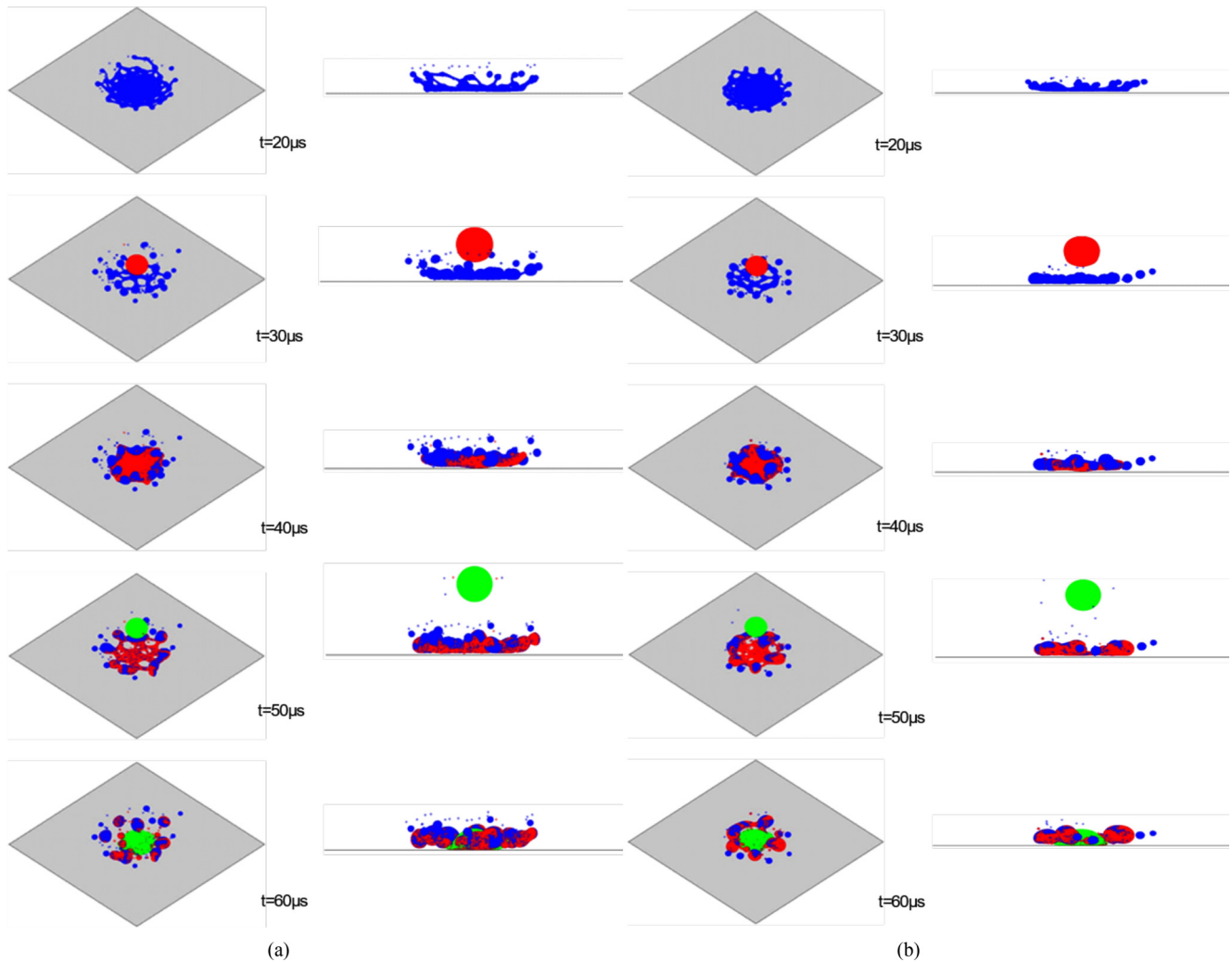
FIG. 7. Postimpingement outcomes at $T_w = 600$ K and $f = 40$ kHz: (a) $P = 5$ bar and (b) $P = 20$ bar.

part merges with the existing film in isolated chunks around the impingement point, as seen at $t = 130$ μs and $t = 150$ μs for $f = 20$ kHz, and at $t = 105$ μs for $f = 30$ kHz. A further increase in the impingement frequency results in succeeding drops impinging on a thin film formed by the preceding drops, generating several secondary droplets. With the quick impingement of subsequent drops, the impact results in isolated chunks of liquid along with the film formed from the recent drop impact at the center, as shown in Fig. 3(a) and Fig. 3(b).

The wall surface temperature of 600 K is above the Leidenfrost temperature. At a temperature above the Leidenfrost temperature, under the present impingement conditions, the impact of an isolated drop is in the lower limit of the "film-splash" regime [10]. The first drop splashes significantly upon impingement. The rapid heat transfer from the wall to the drop decreases the wetting and forms a vapor layer between the wall and the drop. The resulting secondary droplets are raised above the wall caused by the Leidenfrost effects, which promote rebound and splashing. At an impingement frequency of 10 kHz as shown in Fig. 4(a), the second drop meets the rebounding secondary droplets above the wall. Both come down together, merge, spread, produce a few more secondary droplets, and then rebound from the surface.

The second drop's impact does not splash significantly as the first drop does since the rebounding secondary droplets reduce the momentum of the incoming second drop. This process continues with the subsequent drops, and the size of the rebounding secondary droplet keeps increasing with each newly generated droplet. With the increase in impingement frequency to 20 kHz [Fig. 4 (b)], the second drop meets the rebounding droplets just above the wall. Upon impingement, the drop spreads and finally merges into isolated chunks of the secondary droplets above the wall. Unlike the two previous cases, at 30 kHz shown in Fig. 4(c), the second drop finds the droplet film about to be raised above the wall and hence splashes while spreading and gets merged with the secondary droplets found nearby. The splashing becomes more pronounced, forming bigger secondary droplets with further increased impingement frequency, as shown in Fig. 5(a) and Fig. 5(b).

In summary, with the same impinging conditions for the given K parameter, for wall temperatures below the Leidenfrost temperature, increasing the impingement frequency promotes splashing as the succeeding drops impinge either on thin films or scattered films with patches of the exposed wall surface. At low impingement frequency, the succeed-

ing drops meet secondary droplets about to rebound and coalesce into a larger drop. On the contrary, for the wall temperature above the Leidenfrost temperature, for the similar conditions, rebounding is more pronounced at low impingement frequency, whereas film splash with isolated chunks of secondary droplets is more pronounced at high impingement frequencies.

B. Effects of ambient pressure

The Clausius-Clapeyron equation provides an estimation of the boiling temperature corresponding to the change in ambient pressure:

$$\ln\left(\frac{P_2}{P_1}\right) = \frac{h_v}{R}\left(\frac{1}{T_1} - \frac{1}{T_2}\right). \tag{30}$$

Based on this equation, the boiling point of a liquid increases with the rise in ambient pressure. Although such an equation is not available to accurately determine the Leidenfrost temperature, the Leidenfrost temperature has been found to increase with ambient pressure [26,32–35]. This shift in the Leidenfrost temperature leads to the corresponding change in the Leidenfrost phenomenon and hence the wetting regime. With the changes in ambient pressure, there is a shift in the heat-transfer regimes and thus the impact regimes in the drop-wall interactions process. Ahamed *et al.* [32] predicted the increased difficulty in splashing with the rise in the ambient pressure. To investigate the effects of ambient pressure on the impact dynamics of droplet train impingement, the simulation cases were formulated at 5 and 20 bar ambient pressure with an impingement frequency of 40 kHz at 420 and 600 K while keeping all other parameters the same.

Contrary to the postimpingement outcomes at wall temperature of 420 K and impingement frequency of 40 kHz at 1-bar condition shown in Fig. 3(a), the impingement of the first drop on dry wall under $P = 5$ bar and $P = 20$ bar produces very few to no secondary droplets as shown in Fig. 6(a) and Fig. 6(b). The film gets deposited on the wall, spreads to a maximum diameter, and then recoils. This phenomenon is similar to the outcomes seen in drop-wall interactions at wall temperatures below the liquid's saturation temperature [20]. The impingement of the second drop on the thin wall film results in the splashing of secondary droplets from the film. The impingement of the succeeding drops results in similar behaviors along with crown formation, propagation, and then settling down. The film from the most recent drop impact is concentrated inwards. With the increase in ambient pressure, the splashing becomes more difficult with the impingement of the succeeding drops, as seen at corresponding times in Fig. 6(a) and Fig. 6(b). This behavior is caused by the shift in the boiling temperature in accordance with the change in ambient pressure.

Similarly, at 600 K, the increase in the ambient pressure makes it more difficult for disintegration or film splashing as can be seen by comparing Fig. 5(a) and Fig. 7. The secondary droplets are distributed more towards the impingement point as the ambient pressure increases. This results in an easier merging of the film–secondary droplets from incoming drops with the secondary droplets from the preceding drops. Thus, it can be said that the increase in the ambient pressure results in a shift in the Leidenfrost temperature and behaviors, making the splashing and formation of secondary droplets difficult. The impingement of a droplet train results in coalescence with the secondary droplets and film formed from the preceding drops that are distributed randomly above the wall and around the impingement point. Given the same impingement conditions, a further increase in the ambient pressure is expected to result in an inward concentration of the secondary droplets that will merge.

IV. CONCLUSIONS

The SPH method is used to investigate the effects of impingement frequency on the Leidenfrost behaviors for high wall temperatures and elevated ambient pressures. The impact of a stream of *n*-heptane drops is simulated.

Under the atmospheric pressure condition, for wall temperatures below the Leidenfrost temperature, increasing the impingement frequency promotes splashing because of the impingement of the succeeding drops on thin wall films or broken films with exposed wall surfaces. At low impingement frequency, the succeeding drops meet the secondary droplets about to rebound, and both coalesce into a large drop. For the same impingement conditions, with the wall temperature above the Leidenfrost temperature, at low impingement frequencies, recoiling and rebounding of the secondary droplets are seen, along with a few of them being raised above the heated wall. However, at high impingement frequencies, the succeeding drops impinge on thin liquid films about to be raised above the wall by the vapor film formed between the liquid and the wall, thus producing isolated chunks of secondary droplets. Furthermore, the Leidenfrost temperature increases with increased ambient pressure, and there is a shift in the Leidenfrost behavior that guides the wetting regime and film splashing. Splashing becomes more difficult as the ambient pressure increases, and the coalescence of the secondary droplets takes place near the impingement point on consecutive drop impacts. The present study on droplet train impingement under a wide range of wall temperatures and pressures can help develop models to predict drop-wall interactions under high-temperature and high-pressure conditions.

[1] S. Chandra and C. T. Avedisian, Proc. R. Soc. London, Ser. A: Math. Phys. Sci. **432**, 13 (1991).

[2] G. Liang and I. Mudawar, Int. J. Heat Mass Transfer **106**, 103 (2017).

[3] A. Moreira, A. Moita, and M. Panao, Prog. Energy Combust. Sci. **36**, 554 (2010).

[4] S.-C. Kong, Atomization Sprays **17**, 473 (2007).

[5] S. Nukiyama, Int. J. Heat Mass Transfer **9**, 1419 (1966).

[6] K. J. Baumeister and F. F. Simon, J. Heat Transfer **95**, 166 (1973).

[7] J. D. Bernardin and I. Mudawar, J. Heat Transfer **126**, 272 (2004).

[8] J. Lienhard, Chem. Eng. Sci. **31**, 847 (1976).

[9] S.-C. Yao and K. Y. Cai, Exp. Therm. Fluid Sci. **1**, 363 (1988).

[10] Y. Pan, X. Yang, S.-C. Kong, and C.-B. M. Kweon, Atomization Sprays **30**, 153 (2020).

[11] H. J. J. Staat, T. Tran, B. Geerdink, G. Riboux, C. Sun, J. M. Gordillo, and D. Lohse, J. Fluid Mech. **779**, R3 (2015).

[12] A. Karl and A. Frohn, Phys. Fluids **12**, 785 (2000).

[13] G. Cossali, M. Marengo, and M. Santini, in Proceedings of the 9th ICLASS, Sorrento, Italy, 2003.

[14] M. F. Trujillo and S. R. Lewis, Phys. Fluids **24**, 112102 (2012).

[15] L. Qiu, S. Dubey, F. H. Choo, and F. Duan, Appl. Phys. Lett. **107**, 164102 (2015).

[16] C. Mundo, M. Sommerfeld, and C. Tropea, Int. J. Multiphase Flow **21**, 151 (1995).

[17] A. L. Yarin and D. A. Weiss, J. Fluid Mech. **283**, 141 (1995).

[18] D. W. Stanton and C. J. Rutland, Int. J. Heat Mass Transfer **41**, 3037 (1998).

[19] G. Liang and I. Mudawar, Int. J. Heat Mass Transfer **101**, 577 (2016).

[20] K. K. Subedi, S.-C. Kong, and C.-B. M. Kweon, Int. J. Multiphase Flow **151**, 104060 (2022).

[21] J. P. Morris, P. J. Fox, and Y. Zhu, J. Comput. Phys. **136**, 214 (1997).

[22] X. Yang, M. Liu, and S. Peng, Comput. Fluids **92**, 199 (2014).

[23] Y. Xiu-Feng and L. Mou-Bin, Acta Phys. Sinica **61**, 224701 (2012).

[24] J. J. Monaghan, Ann. Rev. Astron. Astrophys. **30**, 543 (1992).

[25] S. Adami, X. Hu, and N. A. Adams, J. Comput. Phys. **229**, 5011 (2010).

[26] X. Yang and S.-C. Kong, Phys. Rev. E **102**, 033313 (2020).

[27] X. Yang and S.-C. Kong, Phys. Rev. E **96**, 033309 (2017).

[28] J. Bonet and T.-S. Lok, Comput. Methods Appl. Mech. Eng. **180**, 97 (1999).

[29] X. Yang, L. Dai, and S.-C. Kong, Proc. Combust. Inst. **36**, 2393 (2017).

[30] Y. Pan, X. Yang, S.-C. Kong, F. C. Ting, C. Iyer, and J. Yi, Int. J. Engine Res. **23**, 416 (2022).

[31] T. Zhang, J. Muthusamy, J. L. Alvarado, A. Kanjirakat, and R. Sadr, International Journal of Heat and Fluid Flow **57**, 24 (2016).

[32] S. Ahamed, Y. Cho, S.-C. Kong, and C.-B. M. Kweon, Atomization and Sprays **32**, 1 (2022).

[33] D. Orejon, K. Sefiane, and Y. Takata, Physical Review E **90**, 053012 (2014).

[34] A. Chausalkar, C.-B. M. Kweon, S.-C. Kong, and J. B. Michael, Int. J. Heat Mass Transfer **153**, 119571 (2020).

[35] G. Emmerson and C. Snoek, Int. J. Heat Mass Transfer **21**, 1081 (1978).